



Technical Note

Identifying Potential Landslides by Stacking-InSAR in Southwestern China and Its Performance Comparison with SBAS-InSAR

Lele Zhang ¹, Keren Dai ^{1,2,*}, Jin Deng ¹, Daqing Ge ³, Rubing Liang ¹, Weile Li ² and Qiang Xu ²

¹ College of Earth Science, Chengdu University of Technology, Chengdu 610059, China; zhangll96@stu.cdut.edu.cn (L.Z.); dengjin@stu.cdut.edu.cn (J.D.); liangrubing@stu.cdut.edu.cn (R.L.)

² State Key Laboratory of Geohazard Prevention and Geoenvironment Protection, Chengdu University of Technology, Chengdu 610059, China; liweile08@mail.cdut.edu.cn (W.L.); xq@cdut.edu.cn (Q.X.)

³ China Aero Geophysical Survey & Remote Sensing, Center for Land and Resources (AGRS), Beijing 100083, China; gedaqing@mail.cgs.gov.cn

* Correspondence: daikeren17@cdut.edu.cn



Citation: Zhang, L.; Dai, K.; Deng, J.; Ge, D.; Liang, R.; Li, W.; Xu, Q. Identifying Potential Landslides by Stacking-InSAR in Southwestern China and Its Performance Comparison with SBAS-InSAR. *Remote Sens.* **2021**, *13*, 3662. <https://doi.org/10.3390/rs13183662>

Academic Editors: Lei Zhang and Zhong Lu

Received: 25 July 2021

Accepted: 9 September 2021

Published: 14 September 2021

Publisher's Note: MDPI stays neutral with regard to jurisdictional claims in published maps and institutional affiliations.



Copyright: © 2021 by the authors. Licensee MDPI, Basel, Switzerland. This article is an open access article distributed under the terms and conditions of the Creative Commons Attribution (CC BY) license (<https://creativecommons.org/licenses/by/4.0/>).

1. Introduction

Landslide disasters occur frequently in the mountainous southwestern region of China, and often cause severe economic losses and even huge casualties [1–5]. Identifying where landslides could happen is important for landslides hazard mitigation. Optical remote sensing is dramatically affected by the clouds and fog in southwestern China. Interferometry Synthetic Aperture Radar (InSAR), with the advantages of all-day, all-weather, cloud-free and high measurement accuracy [6–14], has become a useful tool to identify active slopes, which are probably potential landslides. In the vast steep mountainous region of southwestern China, the fast and accurate identification of potential landslides with the use of cutting-edge InSAR technology is of great significance for subsequent monitoring and early warning to mitigate landslide disasters.

The time series InSAR (TS-InSAR) method (e.g., Persistent Scatterer InSAR (PS-InSAR) [15], Small Baselines Subset InSAR (SBAS-InSAR) [16], and Interferometric Point

target Analysis (IPTA) [17]) overcome the technical problems of low coherence and atmospheric delay, and have been successfully used in monitoring landslide displacement [18–29] and identifying potential landslides [30–32]. However, the conventional TS-InSAR algorithms are relatively time-consuming and labor-intensive, especially for the upcoming massive multi-orbit multi-type SAR data. As a simple and convenient TS-InSAR method, the Stacking-InSAR method has been discussed and used for displacement monitoring [33–35]. In terms of landslide monitoring and early identification, Liu et al. [35] achieved large-scale geohazard identification based on the Stacking-InSAR method with ScanSAR data. Zhang et al. [36] proposed the GACOS-assisted Stacking-InSAR method to identify potential landslides in the Jinshan River Region. Stacking-InSAR and conventional TS-InSAR have been given increasing attention and has been used in wide-area potential landslide identification, with the advantage of fast processing and high accuracy, respectively. However, differences in performance and suitability between Stacking and conventional TS-InSAR methods for potential landslide identification in mountainous areas need to be further identified and understood.

In this paper, we used the Stacking-InSAR method to identify potential landslides along the national highway near Wenchuan County with 40 ascending Sentinel-1 data. High consistency was achieved when comparing Stacking-InSAR results with SBAS-InSAR results. By analyzing missing and different detection, we were able to identify the reasons for the different identification and feasibility of the two methods, which could play an important role in understanding, analyzing and interpreting results for the further application of potential landslide identification by InSAR.

2. Materials and Methods

2.1. Study Area

The study area is located along the national road near Wenchuan County in the southwestern Sichuan Province, China (Figure 1). It is a typical mountainous area with steep slopes near the Longmenshan fault, hit by a heavy Ms. 8.0 earthquake in 2008. The complex geographical environment provides a good environment for the growth of a large number of potential landslides. Therefore, this area is highly susceptible to landslides and other geohazards. There is one main road along the valley, including part of the G213 and G317 China national highways, which is surrounded by steep high mountains on both sides, with the valleys are eroded by Minjing River and Zagunao River (Figure 1a). The area marked with red lines in Figure 1b is the specific study area, with an altitude of about 3000–4000 m, involving four counties: Li County, Wenchuan County, Mao County, and Heishui County. The climate is relatively dry, with heavy rains in summer, leading to the frequent occurrence of natural disasters in this season, such as the landslide in Xinmo Village, Maoxian County in 2017, which had more than 90 casualties [37–42].

2.2. Datasets Used in This Study

Sentinel-1 was launched by the European Space Agency (ESA) in 2014, carrying a C-band SAR with an orbit height of 690 km and a revisiting cycle of 12 days. The main parameters are shown in Table 1. In this study, the single look complex (SLC) format data of the VV polarization mode in the Interferometric Wide (IW) mode were used for Stacking-InSAR processing, and the images were acquired from November 2017 to March 2019. Forty ascending orbit images were used for the analysis, with the temporal baseline and the perpendicular baseline controlled within 60 days and 200 m, respectively. The digital elevation model (DEM) from the shuttle radar topography mission (SRTM) [43] with a spatial resolution of 30 m was used to calculate terrain feature parameters, extract overlay and shadow areas and remove the topographic effect in the InSAR processing.

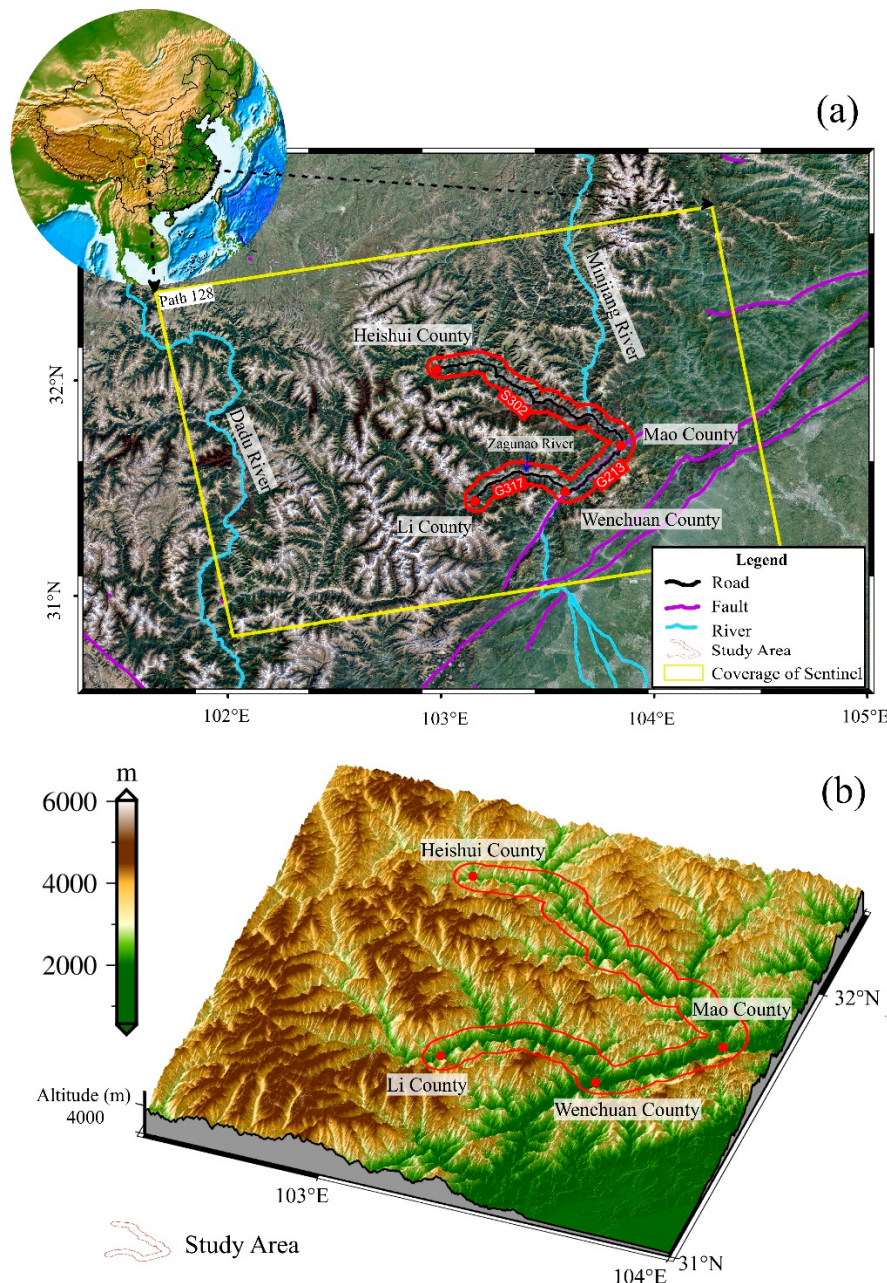


Figure 1. (a) Basic information and location of study area; (b) The terrain and altitude of study area.

Table 1. Main parameters of the Sentinel-1 data used in this study.

Parameter	Value
Temporal coverage	2017.11.27–2019.03.22
Orbital direction	Ascending
Wavelength	5.6 cm
Number of images	40
Azimuth/Range pixel spacing	13.99 m/2.33 m

2.3. Stacking-InSAR Method

The Stacking-InSAR method was originally proposed by Sandwell in 1998 [44]. Although the accuracy of Stacking-InSAR is not as high as the time series InSAR processing (such as PS-InSAR and SBAS-InSAR), it has its own advantages. The Stacking-InSAR

processing was performed in GAMMA software in this study. Specific processing steps are as follows:

As shown in Figure 2, assuming that there were $N + 1$ SAR images covering the study area, the SLC images were acquired and co-registered with external DEM data and precision orbit data. After forming a differential interferometric network with the threshold on perpendicular and temporal baseline, the interferograms were generated. Adaptive filtering and phase unwrapping were performed to acquire a series of unwrapped differential interferograms.

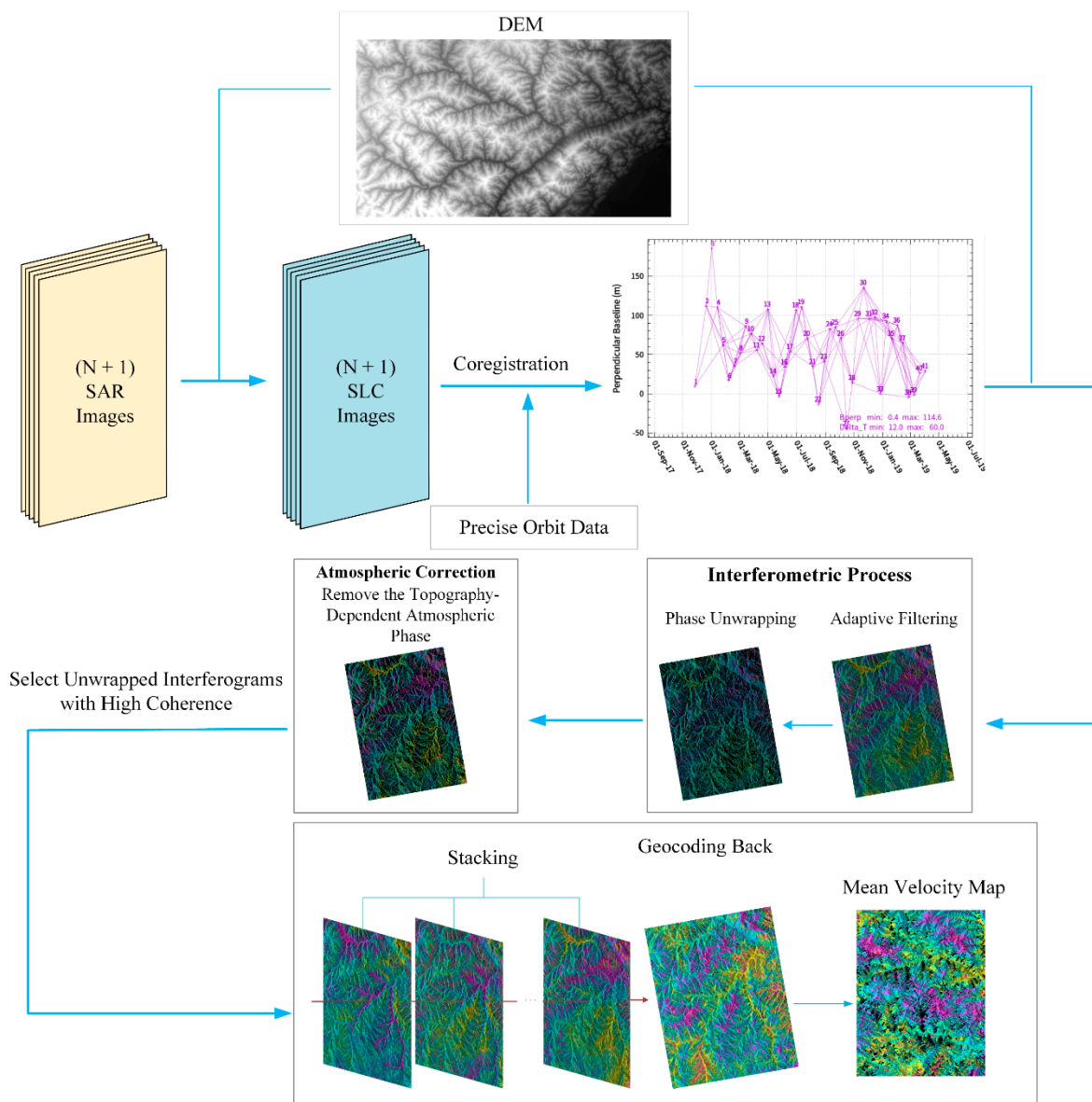


Figure 2. The flow chart of Stacking-InSAR method.

As the study area is in the mountainous area, we used a simple linear model to remove the topography-dependent atmospheric phase [45]. In order to ensure the measurement accuracy of Stacking-InSAR, only the unwrapped interferograms with good coherence were then selected for stacking the unwrapped phase. The algorithm assumes that the displacement of the ground surface changes near linearly, and the phase noise (including

atmospheric phase) in a certain area is random in time. The weight of each interference pair is related to its time interval. Therefore, the displacement phase can be separated as,

$$\bar{\varphi} = \sum_{i=1}^n \varphi_i \cdot \Delta T_i / \sum_{i=1}^n \Delta T_i^2 \quad (1)$$

in which $\bar{\varphi}$ represents the rate of phase change; φ_i and ΔT_i represents the interference phase of the i -th interference image and the time interval of the i -th interference pair, respectively.

Then the average rate of phase change then would be converted to the displacement rate as,

$$V_{disp} = \frac{\lambda \cdot \bar{\varphi}}{4\pi} \quad (2)$$

where V_{disp} is the average displacement rate result along the LOS direction, λ is the radar wavelength, and t_Δ shows the time span. The standard deviation of the average displacement rate can be expressed as,

$$std(V_{disp}) = \sqrt{\frac{1}{n} \cdot \frac{\sum_{i=1}^n \left(\Delta T_i^2 \cdot \left(\frac{\varphi_i}{\Delta T_i} - V_{disp} \right)^2 \right)}{\sum_{i=1}^n \Delta T_i^2}} \quad (3)$$

3. Results

3.1. Stacking-InSAR Identification Results

The Stacking-InSAR results are shown in Figure 3a, with a total of 72 potential landslides clearly identified. It should be noted that the identification of potential landslides is not only based on displacements, but also on the knowledge of landslide morphology. Judging from the Google Earth optical image or DEM, only the active slopes with landslide morphology were defined as potential landslides. Three typical areas were selected and enlarged, as shown in Figure 3b–d. The typical area b is located near the Heishui County reservoir. It can be observed from Figure 3b that a series of potential landslides are distributed on both sides of a reservoir bank. The fluctuation of the reservoir's water in different periods causes slope instability and the revival of ancient landslides, resulting in the dense distribution of active slopes in this area. Among them, Mawo Township landslide is the most active slope, with a displacement of 120 mm/year revealed by Stacking-InSAR. The typical area c is located near Li County and active slopes are found on both sides of the G317 highway. Taoping Township is the most active slope with a displacement rate of 80 mm/year.

The typical area d is located near Feihong Township, Mao County, where the potential landslides are densely distributed. Three potential landslides, (d1, d2 and d3) were selected as the main research objects of field investigations. The Stacking-InSAR results and optical remote sensing images of d1, d2, and d3 are enlarged and shown in Figure 3e,f, in which the active displacements and signs of forming landslides can be clearly observed.

Through the field investigations of these three typical slopes (as shown in Figure 4), some damage cracks on the roads (Figure 4a) are observed in the d1 slope. By visiting residential houses in the deformed area, we found that due to ground deformation the houses had already suffered serious cracks and uneven subsidence (Figure 4b). For the d2 slope, there was sparse vegetation and clear damage could be seen along the road on the slope. Through on-site measurement, maximum displacement reaches 30 cm (Figure 4c,d). The front edge of the d3 slope is relatively broken due to the erosion of the Minjiang River, with obvious sliding phenomena (Figure 4e,f). Evident cracks have appeared in the trailing edge and two flanks, resulting in a high risk of slope failure and even blocking of the Min River.

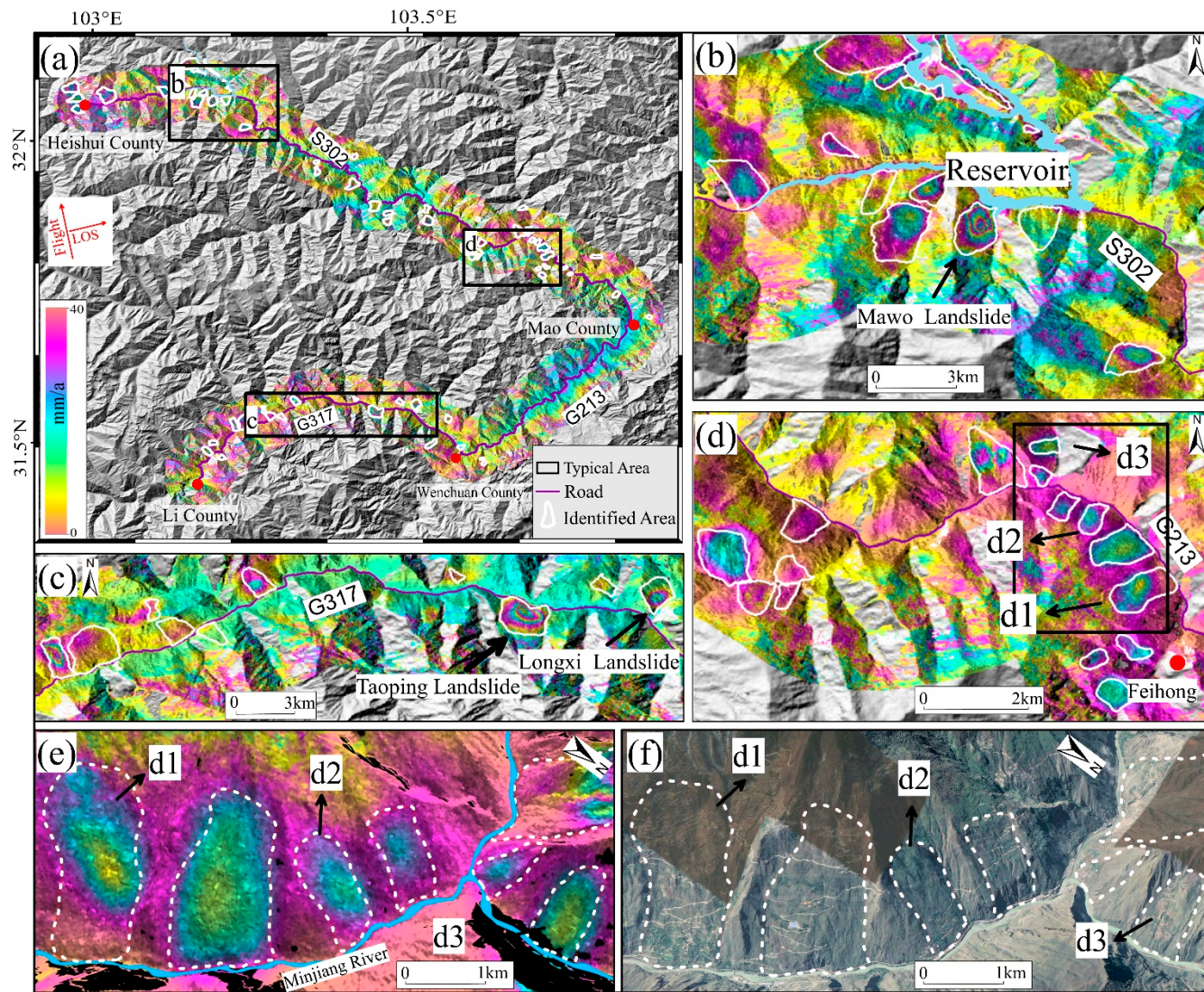


Figure 3. (a) Stacking-InSAR results for the whole study area; (b–d) Enlarged view of the three typical areas in (a); (e,f) Enlarged Stacking-InSAR results and interpretation based on optical remote sensing data of d1, d2 and d3 slopes and surroundings in (d).

3.2. SBAS-InSAR Identification Results

In order to validate and analyze the Stacking-InSAR result, the SBAS-InSAR [16,46] time series method was used to detect active slopes in this area. The SARscape software was used to perform SBAS-InSAR in this study and the results are shown in Figure 5, with a total of 77 potential landslides identified.

For the purpose of comparison, the same typical areas (b, c, d) were selected as in Figure 3, and were enlarged and shown in Figure 5b–d. In general, the identification results of SBAS-InSAR and Stacking-InSAR are highly similar. Among the three key areas, it is obvious from Figures 3b–d and 5b–d that the landslides with high displacement levels (e.g., slopes near Heishui County Reservoir, Taoping Township Landslide and Feihong landslide group) are both presented in the two methods. However, some differences in the results from the two methods can be seen. For example, the Mowa landslide is undetected in the SBAS-InSAR results (Figure 5d), owing to the huge displacement level, a maximum displacement of 120 mm/year.

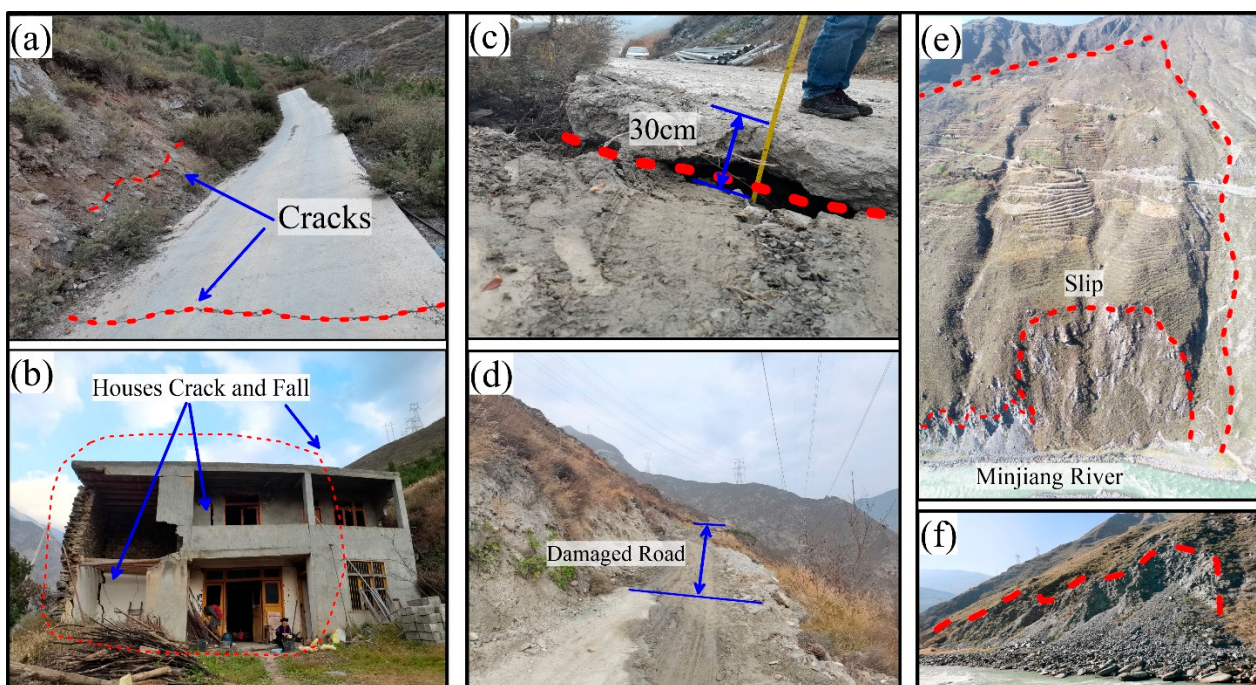


Figure 4. (a,b) Field verification pictures of d1 slope in Figure 3d; (c,d) Field verification pictures of d2 slope in Figure 3d; (e,f) Field verification pictures of d3 slope in Figure 3d.

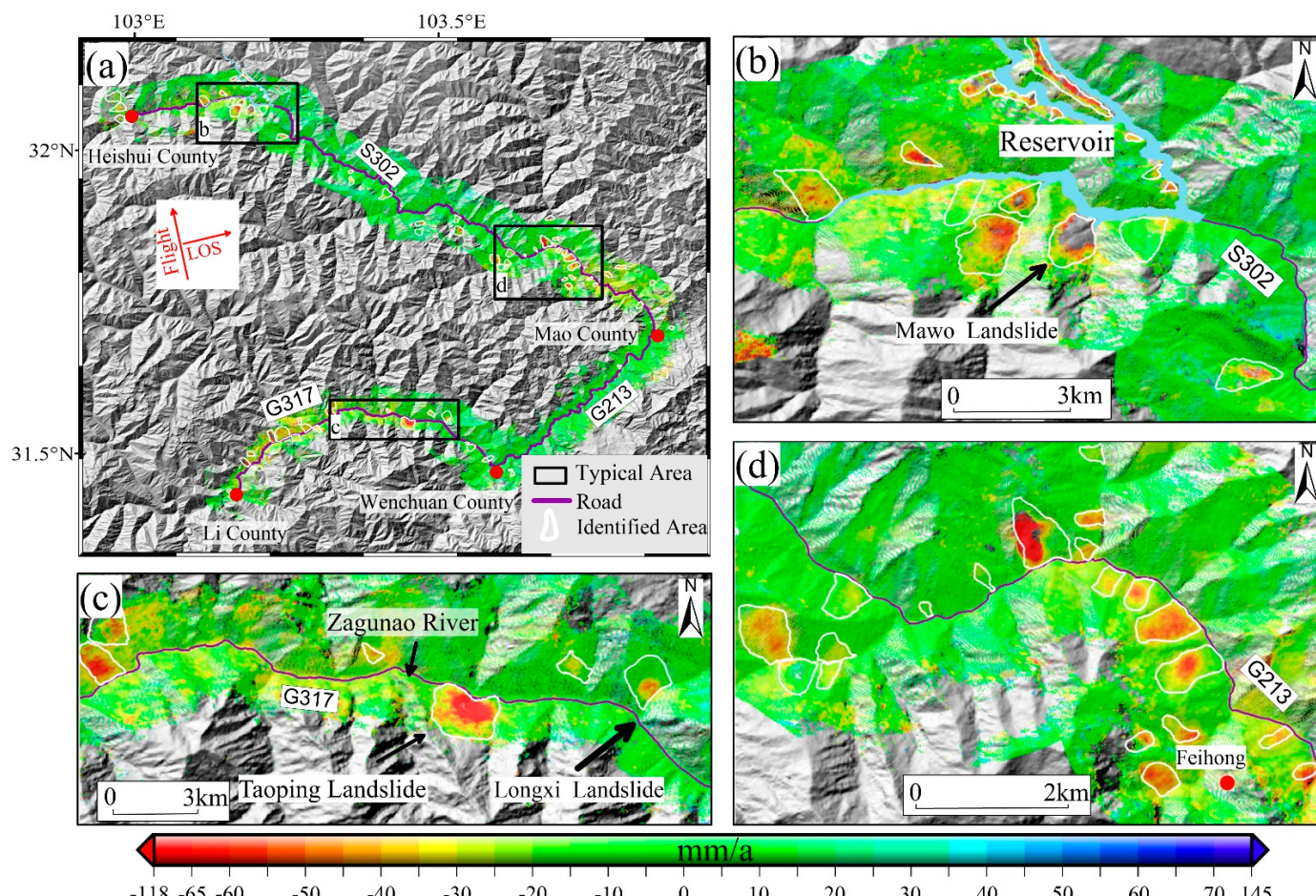


Figure 5. (a) SBAS-InSAR results in the whole study area; (b-d) Enlarged show of the three typical area in (a).

4. Discussion

From a qualitative comparison of Figures 3 and 5, it can be deduced that most of the results from the two methods are consistent. In total, Stacking-InSAR and SBAS-InSAR identified 72 and 77 potential landslides, respectively, of which 67 potential landslides were identified by both methods, indicating a high coincidence. However, there is indeed some difference. Therefore, we performed a detailed and quantitative comparison of the two results, with the statistics shown in Table 2. The total 82 identified potential landslides were divided into three categories according to the identification methods.

Table 2. Statistics and suitability analysis of Stacking-InSAR and SBAS-InSAR results.

Category	Comparison	Count	Displacement Level	Suitability
1	Identified by Both methods	67 (81.7%)	>20 mm/a	Good coherence Large displacement
2	Only by Stacking-InSAR	5 (6.1%)	>20 mm/a	Low coherence Small displacement
3	Only by SBAS-InSAR	10 (12.2%)	<20 mm/a	Small spatial scale Influenced by atmosphere

The first category is potential landslides that can be identified by both methods. Specifically, 67 potential landslides were identified by both Stacking-InSAR and SBAS-InSAR, accounting for 81.7% of all identified landslides. As shown in Figure 6, we zoomed in to two typical areas, the Taoping (Figure 6a–c) and Feihong town landslide groups (Figure 6d–f), which reflect the general conditions for all the 67 potential landslides in category 1. The displacement pattern is highly consistent. The displacement rate along the LOS direction reached more than 65 mm/year and 55 mm/year, respectively. It can be seen that these types of landslides have good coherence with relatively large displacement, resulting in good conditions to be clearly identified by both of the two InSAR methods.

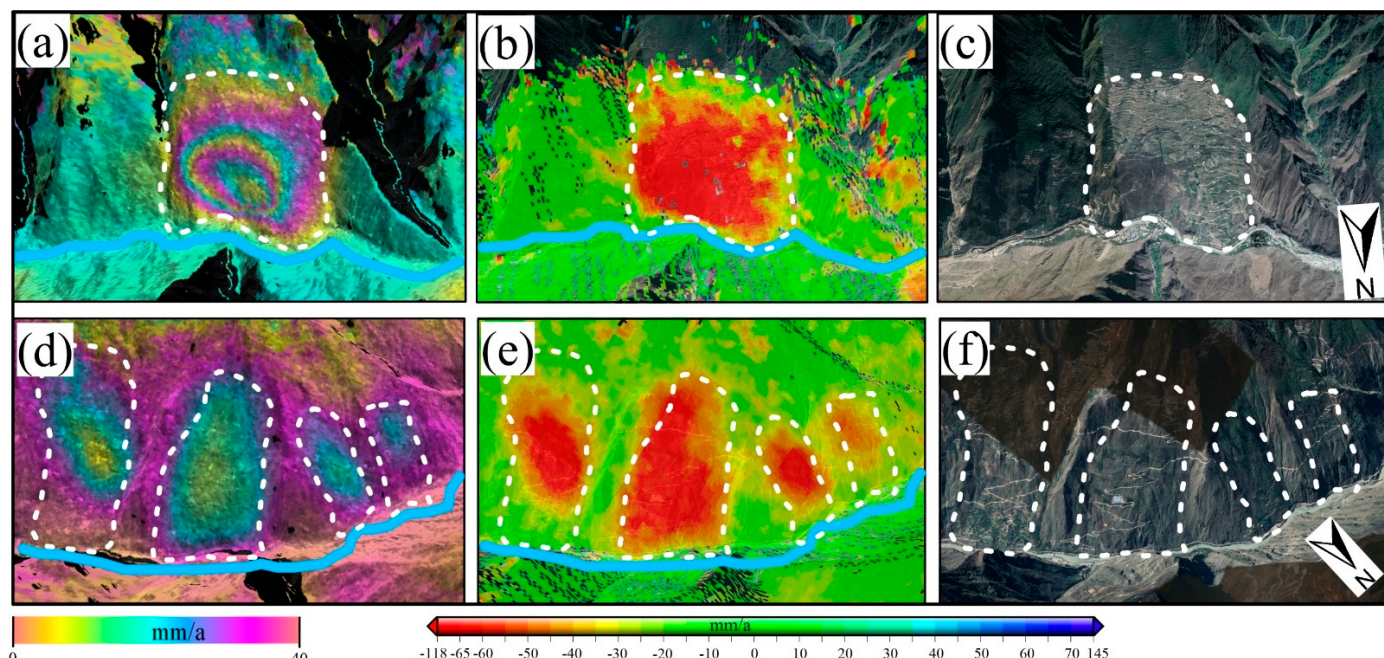


Figure 6. The potential landslides that can be identified by both methods. (a–c) Stacking-InSAR result, SBAS-InSAR result, Google Earth optical image of Taoping landslide, respectively; (d–f) Stacking-InSAR result, SBAS-InSAR result, Google Earth optical image of Taoping Township landslides group, respectively.

The second category is the potential landslides that can only be identified by the Stacking-InSAR method. Most of these landslides have low coherence and are totally decorrelated in the SBAS-InSAR as shown in Figure 7.

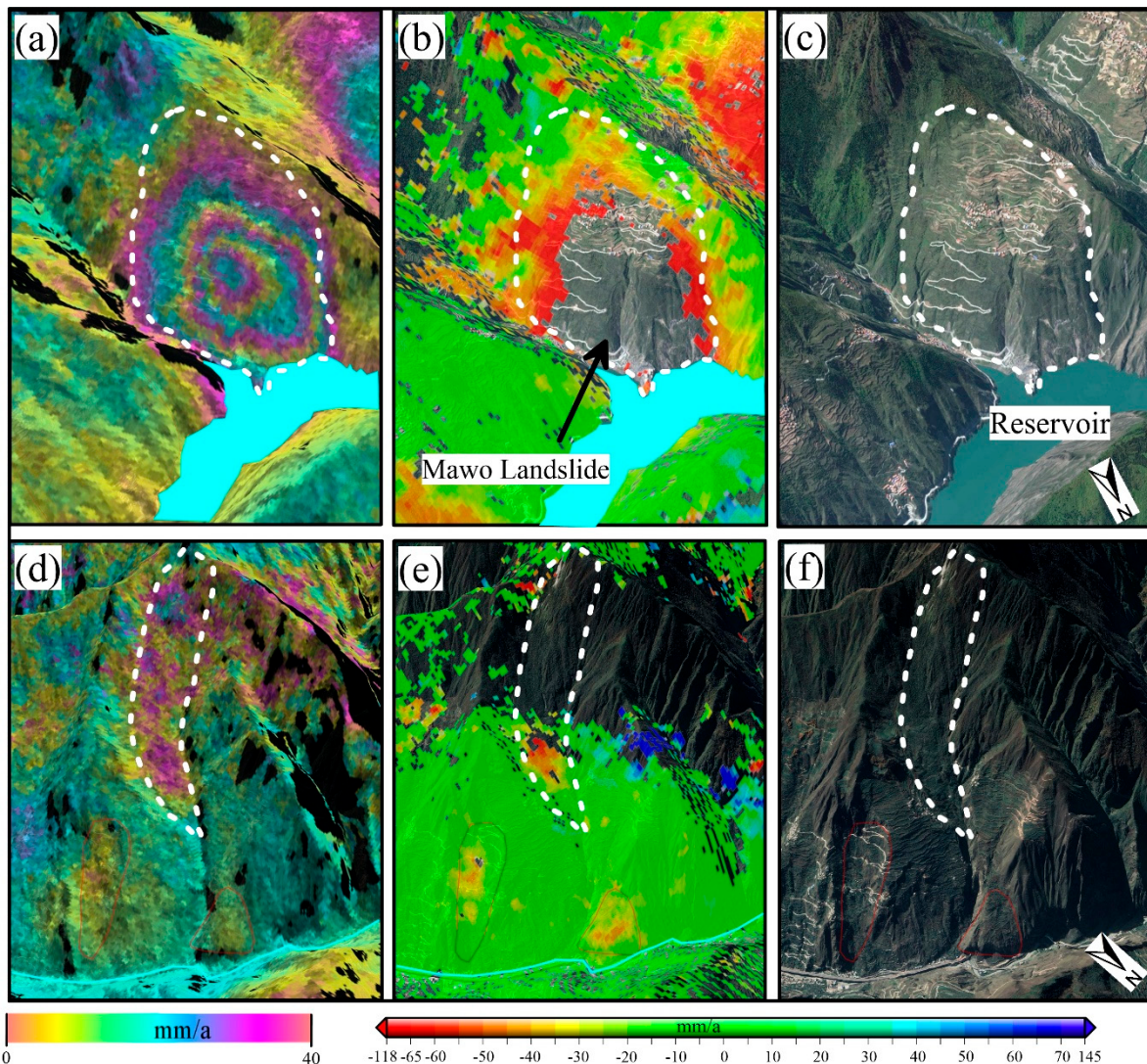


Figure 7. The potential landslides that can only be identified by Stacking-InSAR method. (a,d) Stacking-InSAR results; (b,e) SBAS-InSAR result; (c,f) Google Earth optical image.

As shown in Figure 7a–c, Stacking-InSAR results show that, for the MAWO landslide, LOS displacement has exceeded 120 mm/year (Figure 7a), while SBAS-InSAR produced no result (no coherent points) in the core area of this landslide (Figure 7b). In the second case (Figure 7d–f), the dense vegetation (can be seen from Figure 7f) on the surface of the slope lead to decorrelation, resulting in the absence of displacements results from SBAS-InSAR (Figure 7e), while these displacement areas were identified by Stacking-InSAR (Figure 7d). The main reason for this is that in SBAS-InSAR processing there are strict rules (such as low amplitude dispersion index, high coherence coefficient) for the selection of coherent points, which should maintain high coherence or stable amplitude throughout the whole time span [47]. In this case, the decorrelation, caused by large displacement and poor coherence, lead to the absence of highly coherent points in this area throughout the whole time span. Since Stacking-InSAR just superimposes some of the high unwrapped interferograms to average the phases, the displacement can be retained. It should be noted that there are some displacements on the right of the potential landslide identified in Figure 7d. Judging

from the optical remote sensing image, we did not count this area as potential landslides according to the basic landslides morphology (the displacements may be down to snow melt in the mountain peaks or vegetation).

Therefore, for regions with poor coherence, Stacking-InSAR can retain the displacement and perform better compared with SBAS-InSAR. This point is an important advantage of Stacking-InSAR, which provides more observation and information in terms of spatial scale. It could play an important role in landslide identification by InSAR in mountainous area with dense vegetation.

The third category contains the kinds of potential landslides that can only be identified by the SBAS-InSAR method. As shown in Figure 8a–c, the displacement on this slope only reaches 25 mm/year. There are no clear signs of displacement in the Stacking-InSAR result (Figure 8a), while it can be detected in the SBAS-InSAR result (Figure 8b). This displacement is consistent with the potential landslides identified by the optical image in Figure 8c, where the leading edge of the deformed area has slipped for a long time. Therefore, SBAS-InSAR has a better performance for landslides with small displacement.

In another two cases (Figure 8d–i), atmospheric impacts were revealed. As shown in the white dashed area in Figure 8d,g, wide but vague displacement can be seen in Figure 8d,g. However, this does not match the shape of the terrain on the optical image in Figure 8f,i, which looks similar to the characteristics of the atmosphere. In order to verify this, we extracted the displacement and elevation along two profile lines, AB and CD, in Figure 8d,g, respectively (shown in Figure 8j–k). It is obvious that there is a strong correlation between displacement and elevation along both profiles AB and CD. This is typical of the elevation-dependent atmosphere in mountainous areas, which is correlation in time and space, and cannot be removed by Stacking-InSAR. The corresponding results from SBAS-InSAR in Figure 8e, h reveal the small displacement (about 30 mm/year), as SBAS-InSAR could model and remove the atmosphere effect to some degree.

It should be noted that there is an active area with a small spatial scale (about 160 m in Figure 8i) revealed by SBAS-InSAR in the bottom left corner of Figure 8h, while there is no sign in the Stacking-InSAR result even of displacement reaching up to 30 mm/year. This displacement is verified and can be clearly seen in the optical remote sensing image (Figure 8i). It was suggested that some displacements at small spatial scales are eliminated during the Stacking-InSAR phase accumulation and averaging process, and that SBAS-InSAR performs better in the detection of slopes with small spatial displacement, and small displacement influenced by the atmosphere. All the suitability analysis from the above are summarized in Table 2.

Based on the analysis above, the performance for both two methods affected by some technical features were analyzed and revealed. In addition to performance, some other advantages of Stacking-InSAR should be mentioned and emphasized. The processing time for the Stacking-InSAR and SBAS-InSAR are about 5 min and 5 h (from unwrapped interferograms to the final geocoded displacements results), respectively, revealing a very high efficiency of the Stacking-InSAR method. This could promote deep exploration and application of the coming SAR data with very short revisiting time. Moreover, compared to SBAS-InSAR and other time series InSAR (e.g., PS-InSAR, IPTA), Stacking-InSAR processing is a relatively well-proven algorithm with high efficiency and low technical requirements, which means it is easier to promote and apply in engineering applications.

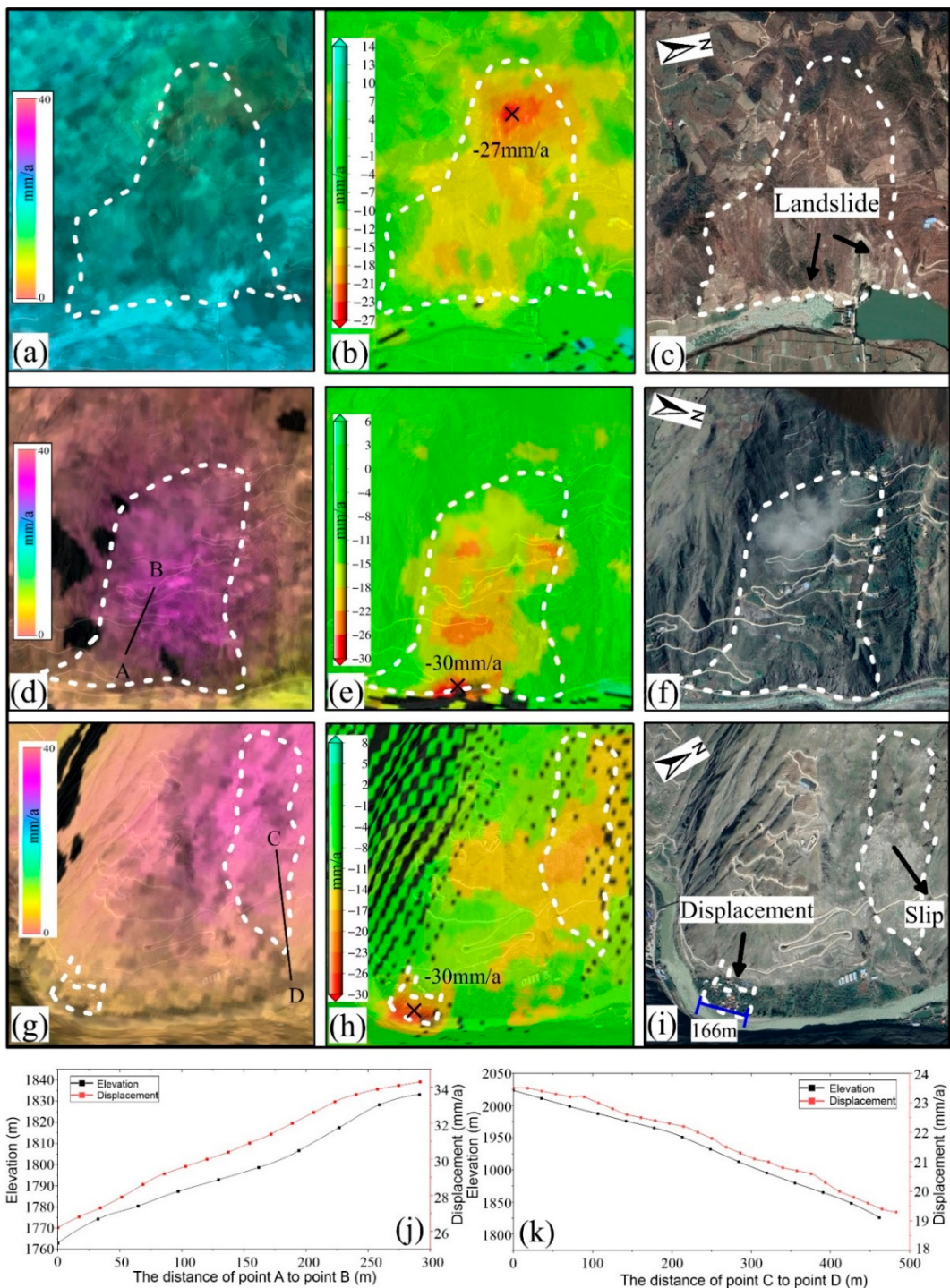


Figure 8. The potential landslides that can only be identified by SBAS-InSAR method. (a,d,g) Stacking-InSAR results; (b,e,h) SBAS-InSAR result; (c,f,i) Google Earth optical image; (j,k) The profile of AB and CD in (d,g), respectively.

5. Conclusions

The national highway near Wenchuan County is located in the Longmen Mountain fault zone, surrounded by steep mountain and valleys. This paper used the Stacking-InSAR method to quickly and accurately identify active slopes based on 40 Sentinel-1 SAR data. As a result, 72 potential landslides were detected, and field investigations were performed. Consistent validation results were achieved indicating that Stacking-InSAR has

the advantages of high efficiency to quickly identify potential landslides in the processing of massive amounts of SAR data.

Moreover, its performance in comparison to SBAS-InSAR was investigated. SBAS-InSAR detected 77 potential landslides, and 67 of them were the same as those detected by Stacking-InSAR, accounting for 81.7% of the total 82 detected active slopes. There were 5 and 10 slopes that could only be identified by Stacking-InSAR and SBAS-InSAR, respectively. We analyzed this difference in detail, revealing the performance and suitability of these two methods with the conclusion that (1) slopes with good coherence and relatively large displacement can be identified by both of the two methods; (2) the Stacking-InSAR method would have better performance for low coherence areas; (3) for slopes with small amounts of displacement, small spatial scales or influence from the atmosphere, SBAS-InSAR would be the best option for the identification of active slopes. The performance and suitability of Stacking-InSAR, mean that it would be an effective and powerful method to qualitatively identify potential landslides, with the advantages of high efficiency, low technical requirements, low computational labor and high spatial observation, and it could play an important role in the future.

Author Contributions: Conceptualization, K.D. and D.G.; Data curation, L.Z. and J.D.; Investigation, R.L.; Methodology, L.Z., J.D., D.G. and W.L.; Project administration, Q.X.; Visualization, R.L.; Writing—original draft, L.Z.; Writing—review & editing, K.D. All authors have read and agreed to the published version of the manuscript.

Funding: This work was funded by the National Natural Science Foundation of China Major Program (41941019), National Natural Science Foundation of China (41801391), the State Key Laboratory of Geohazard Prevention and Geoenvironment Protection Independent Research Project (SKLGP2020Z012), the project on identification and monitoring of potential geological hazards with remote sensing in Sichuan Province (510201202076888) and the Everest Scientific Project at Chengdu University of Technology (2020ZF114103).

Conflicts of Interest: The authors declare no conflict of interest.

References

- Li, W.; Xu, Q.; Lu, H.; Dong, X.; Zhu, Y. Tracking the Deformation History of Large-Scale Rocky Landslides and Its Enlightenment. *Geomat. Inf. Sci. Wuhan Univ.* **2019**, *44*, 1043–1053, 1671–8860. [[CrossRef](#)]
- Chen, X.; Zhou, Q.; Ran, H.; Dong, R. Earthquake-triggered landslides in southwest China. *Nat. Hazards Earth Syst. Sci.* **2012**, *12*, 351–363. [[CrossRef](#)]
- Meng, W.; Xu, Y.; Cheng, W.; Arulrajah, A. Landslide Event on 24 June in Sichuan Province, China: Preliminary Investigation and Analysis. *Geosciences* **2018**, *8*, 39. [[CrossRef](#)]
- Yin, Y.; Wang, F.; Sun, P. Landslide hazards triggered by the 2008 Wenchuan earthquake, Sichuan, China. *Landslides* **2009**, *6*, 139–152. [[CrossRef](#)]
- Scaringi, G.; Fan, X.; Xu, Q.; Liu, C.; Ouyang, C.; Domènec, G.; Yang, F.; Dai, L. Some considerations on the use of numerical methods to simulate past landslides and possible new failures: The case of the recent Xinmo landslide (Sichuan, China). *Landslides* **2018**, *15*, 1359–1375. [[CrossRef](#)]
- Canuti, P.; Casagli, N.; Ermini, L.; Fanti, R.; Farina, P. Landslide activity as a geoindicator in Italy: Significance and new perspectives from remote sensing. *Environ. Geol.* **2004**, *45*, 907–919. [[CrossRef](#)]
- Metternicht, G.; Hurni, L.; Gogu, R. Remote sensing of landslides: An analysis of the potential contribution to geo-spatial systems for hazard assessment in mountainous environments. *Remote Sens. Environ.* **2005**, *98*, 284–303. [[CrossRef](#)]
- Van Westen, C.; Castellanos, E.; Kuriakose, S. Spatial data for landslide susceptibility, hazard, and vulnerability assessment: An overview. *Eng. Geol.* **2008**, *102*, 112–131. [[CrossRef](#)]
- Casagli, N.; Catani, F.; Del Ventisette, C.; Luzi, G. Monitoring, prediction, and early warning using ground-based radar interferometry. *Landslides* **2010**, *7*, 291–301. [[CrossRef](#)]
- Ye, X.; Kaufmann, H.; Guo, X. Landslide Monitoring in the Three Gorges Area Using D-INSAR and Corner Reflectors. *Photogramm. Eng. Remote Sens.* **2004**, *70*, 1167–1172. [[CrossRef](#)]
- Li, Z.; Song, C.; Yu, C.; Xiao, R.; Chen, L.; Luo, H.; Dai, K.; Ge, D.; Ding, Y.; Zhang, Y.; et al. Application of Satellite Radar Remote Sensing to Landslide Detection and Monitoring: Challenges and Solutions. *Geomat. Inf. Sci. Wuhan Univ.* **2019**, *44*, 967–979. [[CrossRef](#)]
- Dong, J.; Zhang, L.; Li, M.; Yu, Y.; Liao, M.; Gong, J.; Luo, H. Measuring precursory movements of the recent Xinmo landslide in Mao County, China with Sentinel-1 and ALOS-2 PALSAR-2 datasets. *Landslides* **2017**, *15*, 135–144. [[CrossRef](#)]

13. Singleton, A.; Li, Z.; Hoey, T.; Muller, J. Evaluating sub-pixel offset techniques as an alternative to D-InSAR for monitoring episodic landslide movements in vegetated terrain. *Remote Sens. Environ.* **2014**, *147*, 133–144. [[CrossRef](#)]
14. Schlögel, R.; Doubre, C.; Malet, J.; Masson, F. Landslide deformation monitoring with ALOS/PALSAR imagery: A D-InSAR geomorphological interpretation method. *Geomorphology* **2015**, *231*, 314–330. [[CrossRef](#)]
15. Ferretti, A.; Prati, C.; Rocca, F. Nonlinear subsidence rate estimation using permanent scatterers in differential SAR interferometry. *IEEE Trans. Geosci. Remote Sens.* **2000**, *38*, 2202–2212. [[CrossRef](#)]
16. Berardino, P.; Fornaro, G.; Lanari, R.; Sansosti, E. A new algorithm for surface deformation monitoring based on small baseline differential SAR interferograms. *IEEE Trans. Geosci. Remote. Sens.* **2002**, *40*, 2375–2383. [[CrossRef](#)]
17. Wegmüller, U.; Werner, C.; Strozzi, T.; Wiesmann, A.; Frey, O.; Santoro, M. Sentinel-1 Support in the GAMMA Software. *Procedia Comput. Sci.* **2016**, *100*, 1305–1312. [[CrossRef](#)]
18. Chen, L.; Zhao, C.; Li, B.; He, K.; Ren, C.; Liu, X.; Liu, D. Deformation monitoring and failure mode research of mining-induced Jianshanying landslide in karst mountain area, China with ALOS/PALSAR-2 images. *Landslides* **2021**, *18*, 2739–2750. [[CrossRef](#)]
19. Dai, K.; Li, Z.; Xu, Q.; Burgmann, R.; Milledge, D.; Tomas, R.; Fan, X.; Zhao, C.; Liu, X.; Peng, J.; et al. Entering the Era of Earth Observation-Based Landslide Warning Systems: A Novel and Exciting Framework. *IEEE Geosci. Remote Sens. Mag.* **2020**, *8*, 136–153. [[CrossRef](#)]
20. Dai, K.; Li, Z.; Tomás, R.; Liu, G.; Yu, B.; Wang, X.; Cheng, H.; Chen, J.; Stockamp, J. Monitoring activity at the Daguangbao mega-landslide (China) using Sentinel-1 TOPS time series interferometry. *Remote Sens. Environ.* **2016**, *186*, 501–513. [[CrossRef](#)]
21. Liao, M.; Tang, J.; Wang, T.; Balz, T.; Zhang, L. Landslide monitoring with high-resolution SAR data in the Three Gorges region. *Sci. China Earth Sci.* **2011**, *55*, 590–601. [[CrossRef](#)]
22. Raspini, F.; Ciampalini, A.; Del Conte, S.; Lombardi, L.; Nocentini, M.; Gigli, G.; Ferretti, A.; Casagli, N. Exploitation of Amplitude and Phase of Satellite SAR Images for Landslide Mapping: The Case of Montescaglioso (South Italy). *Remote Sens.* **2015**, *7*, 14576–14596. [[CrossRef](#)]
23. Sun, Q.; Zhang, L.; Ding, X.; Hu, J.; Li, Z.; Zhu, J. Slope deformation prior to Zhouqu, China landslide from InSAR time series analysis. *Remote Sens. Environ.* **2015**, *156*, 45–57. [[CrossRef](#)]
24. Zhao, C.; Zhang, Q.; He, Y.; Peng, J.; Yang, C.; Kang, Y. Small-scale loess landslide monitoring with small baseline subsets interferometric synthetic aperture radar technique—case study of Xingyuan landslide, Shaanxi, China. *J. Appl. Remote Sens.* **2016**, *10*, 026030. [[CrossRef](#)]
25. Oliveira, S.C.; Zézere, J.; Catalão, J.; Nico, G. The contribution of PSInSAR interferometry to landslide hazard in weak rock-dominated areas. *Landslides* **2014**, *12*, 703–719. [[CrossRef](#)]
26. Tantianuparp, P.; Shi, X.; Zhang, L.; Balz, T.; Liao, M. Characterization of Landslide Deformations in Three Gorges Area Using Multiple InSAR Data Stacks. *Remote Sens.* **2013**, *5*, 2704–2719. [[CrossRef](#)]
27. Zhang, Y.; Meng, X.; Jordan, C.; Novellino, A.; Dijkstra, T.; Chen, G. Investigating slow-moving landslides in the Zhouqu region of China using InSAR time series. *Landslides* **2018**, *15*, 1299–1315. [[CrossRef](#)]
28. Nikolaeva, E.; Walter, T.; Shirzaei, M.; Zschau, J. Landslide observation and volume estimation in central Georgia based on L-band InSAR. *Nat. Hazards Earth Syst. Sci.* **2014**, *14*, 675–688. [[CrossRef](#)]
29. Hu, B.; Chen, J.; Zhang, X. Monitoring the Land Subsidence Area in a Coastal Urban Area with InSAR and GNSS. *Sensors* **2019**, *19*, 3181. [[CrossRef](#)]
30. Liu, P.; Li, Z.; Hoey, T.; Kincaid, C.; Zhang, J.; Zeng, Q.; Muller, J. Using advanced InSAR time series techniques to monitor landslide movements in Badong of the Three Gorges region, China. *Int. J. Appl. Earth Obs. Geoinf.* **2013**, *21*, 253–264. [[CrossRef](#)]
31. Zhao, C.; Kang, Y.; Zhang, Q.; Lu, Z.; Li, B. Landslide Identification and Monitoring along the Jinsha River Catchment (Wudongde Reservoir Area), China, Using the InSAR Method. *Remote Sens.* **2018**, *10*, 993. [[CrossRef](#)]
32. Wang, G.; Wang, Y.; Zang, X.; Zhu, J.; Wu, W. Locating and monitoring of landslides based on small baseline subset interferometric synthetic aperture radar. *J. Appl. Remote Sens.* **2019**, *13*, 44528. [[CrossRef](#)]
33. Novali, F.; Eyal, Y.; Baer, G.; Nof, R. Current surface displacement along the Carmel Fault system in Israel from InSAR stacking and PSInSAR. *Isr. J. Earth Sci.* **2008**, *57*, 71–86. [[CrossRef](#)]
34. Dai, K.; Liu, G.; Li, Z.; Ma, D.; Wang, X.; Zhang, B.; Tang, J.; Li, G. Monitoring Highway Stability in Permafrost Regions with X-band Temporary Scatterers Stacking InSAR. *Sensors* **2018**, *18*, 1876. [[CrossRef](#)]
35. Liu, B.; Ge, D.; Wang, S.; Li, M.; Zhang, L.; Wang, Y.; Wu, Q. Combining Application of TOPS and ScanSAR InSAR in Large-Scale Geohazards Identification. *Geomat. Inf. Sci. Wuhan Univ.* **2020**, *45*, 1756–1762. [[CrossRef](#)]
36. Zhang, C.; Li, Z.; Yu, C.; Song, C.; Xiao, R.; Peng, J. Landslide Detection: GACOS-assisted InSAR Stacking and Its Application to the Jinsha River Region. *Geomat. Inf. Sci. Wuhan Univ.* **2020**, *1*–16. [[CrossRef](#)]
37. Xu, Q.; Li, W.; Dong, X.; Xiao, X.; Fan, X.; Pei, X. The Xinmocun landslide on June 24, 2017 in Maoxian, Sichuan: Characteristics and failure mechanism. *Chin. J. Rock Mech. Eng.* **2017**, *36*, 2612–2628. [[CrossRef](#)]
38. Hu, K.; Wu, C.; Tang, J.; Pasuto, A.; Li, Y.; Yan, S. New understandings of the June 24th 2017 Xinmo Landslide, Maoxian, Sichuan, China. *Landslides* **2018**, *15*, 2465–2474. [[CrossRef](#)]
39. Dai, K.; Xu, Q.; Li, Z.; Tomás, R.; Fan, X.; Dong, X.; Li, W.; Zhou, Z.; Gou, J.; Ran, P. Post-disaster assessment of 2017 catastrophic Xinmo landslide (China) by spaceborne SAR interferometry. *Landslides* **2019**, *16*, 1189–1199. [[CrossRef](#)]
40. Intrieri, E.; Raspini, F.; Fumagalli, A.; Lu, P.; Del Conte, S.; Farina, P.; Allievi, J.; Ferretti, A.; Casagli, N. The Maoxian landslide as seen from space: Detecting precursors of failure with Sentinel-1 data. *Landslides* **2017**, *15*, 123–133. [[CrossRef](#)]

41. Fan, X.; Xu, Q.; Scaringi, G.; Dai, L.; Li, W.; Dong, X.; Zhu, X.; Pei, X.; Dai, K.; Havenith, H. Failure mechanism and kinematics of the deadly June 24th 2017 Xinmo landslide, Maoxian, Sichuan, China. *Landslides* **2017**, *14*, 2129–2146. [[CrossRef](#)]
42. Ouyang, C.J.; Zhao, W.; He, S.; Wang, D.; Zhou, S.; An, H.; Wang, Z.; Cheng, D. Numerical modeling and dynamic analysis of the 2017 Xinmo landslide in Maoxian County, China. *J. Mt. Sci.* **2017**, *14*, 1701–1711. [[CrossRef](#)]
43. Farr, T.; Rosen, P.; Caro, E.; Crippen, R.; Duren, R.; Hensley, S.; Kobrick, M.; Paller, M.; Rodriguez, E.; Roth, L.; et al. The Shuttle Radar Topography Mission. *Rev. Geophys.* **2007**, *45*. [[CrossRef](#)]
44. Sandwell, D.; Price, E. Phase gradient approach to stacking interferograms. *J. Geophys. Res. Solid Earth* **1998**, *103*, 30183–30204. [[CrossRef](#)]
45. Li, Z.; Ding, X.; Huang, C.; Wadge, G.; Zheng, D. Modeling of atmospheric effects on InSAR measurements by incorporating terrain elevation information. *J. Atmos. Sol.-Terr. Phys.* **2006**, *68*, 1189–1194. [[CrossRef](#)]
46. Casu, F.; Manzo, M.; Lanari, R. A quantitative assessment of the SBAS algorithm performance for surface deformation retrieval from DInSAR data. *Remote Sens. Environ.* **2006**, *102*, 195–210. [[CrossRef](#)]
47. Tizzani, P.; Berardino, P.; Casu, F.; Euillades, P.; Manzo, M.; Ricciardi, G.; Zeni, G.; Lanari, R. Surface deformation of Long Valley caldera and Mono Basin, California, investigated with the SBAS-InSAR approach. *Remote Sens. Environ.* **2007**, *108*, 277–289. [[CrossRef](#)]